ORIGINAL RESEARCH

Experimental study of a new pure bending yielding dissipater

Hassan Zibasokhan[1] · Farhad Behnamfar[1] · Mojtaba Azhari[1]

Abstract

In this paper, a new yielding dissipater device is introduced for seismic protection of concentrically braced structures. The device is fabricated by a set of transverse plates inserted in the middle of a diagonal brace. The special configuration of the new device transforms the axial force of a concentric brace to pure bending in the dissipater plates. The dissipater plates are designed to bend inelastically over their whole surface to dissipate energy. Welding is avoided in the dissipater plates and consequently the ductile behavior of steel results in a good hysteric behavior of the new device. Experimental results of sixteen specimens of the proposed dissipater device show a stable hysteretic behavior of the brace and similar behavior in tension and compression. An analytical model is developed and verified to predict the behavior of the proposed dissipater.

List of symbols

a	Side part length of the plates
b	Middle part length of the plates
c	Width of the plates
C_p	Overstrength factor
E	Modulus of elasticity
E*	Second branch modulus
F_y	Nominal yield stress
F_{ye}	Expected yield stress
F_u	Ultimate stress
I	Moment of inertia
k_i	Initial axial stiffness
$k_{i,ex}$	Experimental initial axial stiffness
L	Total length of the plates
M	Bending moment in the middle part
n	Number of dissipater plates

✉ Farhad Behnamfar
    farhad@cc.iut.ac.ir

[1] Department of Civil Engineering, Isfahan University of Technology, Esfahan 8415683111, Iran

Published online: 09 April 2019

P	Axial force
P_{design}	Axial design capacity
P_y	Axial yield strength
P_u	Axial ultimate capacity
$P_{y,ex}$	Experimental yield strength
$P_{t,ex}$	Experimental tensile strength
$P_{c,ex}$	Experimental compressive strength
$P_{ex,80}$	Experimental capacity corresponding to 80 mm displacement
R	Radius of curvature in middle part
R_y	Material overstrength factor
t	Thickness of dissipater plates
α	Transverse curvature constraint coefficient
β	Movement restriction coefficient
γ	Coefficient for calibration of ε_r
δ_y	Yield displacement
$\delta_{y,ex}$	Experimental yield displacement
$\delta_{max,ex}$	Maximum experimental displacement
δ_u	Ultimate displacement
Δ	Displacement of the device
Δ_1	Side part displacement caused by support rotation
Δ_2	Side part displacement caused by deflection
Δ_{axial}	Axial displacement
Δ_P	Slippage of the dissipater plates on the middle support
ε_0	Maximum strain in the middle part
ε_y	Yield strain
ε_r	Strain corresponding to beginning of movement restriction
ε_u	Strain corresponding to ultimate stress
$\theta_{support}$	Plate rotation at the middle support
$\theta_{support,80}$	Plate rotation at the middle support at 80 mm displacement
λ	Coefficient for calibration of β
υ	Poisson's ratio
φ	Angle of strain plane of the section

1 Introduction

Structural control systems are mainly used to reduce damages of structures in earthquakes. These systems have been developed significantly over the last few decades. They can be broadly classified into three categories: (1) passive control systems that are structures equipped with devices which do not need an external source of energy, (2) active control systems that are structures equipped with processing sensors and force transfer devices which need an external source of energy to work, and (3) semi-active control systems which need little external energy to change structural characteristics (Cheng et al. 2008). The use of dissipaters, especially yielding dissipaters, is one of the most popular structural control methods. The yielding dissipaters have been widely considered for their advantages including low cost, simple manufacturing technology, simple and fast substitution after earthquakes and temperature independency at normal temperatures. The yielding

dissipaters dissipate significant amounts of energy in each cycle of inelastic deformation and prevent damage in other members of structure (Soong and Dargush 1997).

A large number of existing dissipater devices are subjected to a combination of axial, shear, torsional, and flexural actions that causes yielding of the ductile part of the dissipater. But usually only one of these internal actions is considered as the main factor to be the cause of yielding. In the buckling restrained braces, the axial force causes yielding of the restrained core (Black et al. 2004; Piedrafita et al. 2013, 2015; Tabatabaei et al. 2014; Ozcelik et al. 2017). To solve the problem of high yielding forces and relatively small longitudinal strain toleration in these dissipaters, some methods have been suggested by various researchers (Piedrafita et al. 2013; Tabatabaei et al. 2014). Other types of axially yielding members have also been developed (Speicher et al. 2011; Calado et al. 2013). In the dissipater device with a dominant shear mechanism, the shear force yields a significant portion of the material simultaneously, which is considered as a desirable way to cause yielding in metals (Nakashima et al. 1994). The mentioned dissipaters suffer from shear buckling before yielding as a major problem. Several suggestions have been made to suppress this problem, including use of horizontal and vertical stiffened shear plates (Nakashima et al. 1994), shear plates with slit (Hitaka and Matsui 2003), perforated shear plates (Chan et al. 2013; Formisano et al. 2016), and buckling restrained shear panels (Deng et al. 2015). Creating a torsional moment in a member can be a cause for yielding. Among the researches, use of rectangular plates or pipe sections under torsional moment (Skinner et al. 1975; Franco et al. 2010), and use of pipe section in braced frames as a yielding dissipater (Vetr and Ghamari 2012), can be mentioned as well. The main problem with these types of dissipaters is the simultaneous presence of shear force and torsion at the section, which prevents complete use of energy dissipation capacity of the material. On the other hand, use of a bending moment to provide for yielding is one of the most popular mechanisms in dissipater devices. Many suggestions have been made to make use of plates with bending moment as a dissipater, including use of x-shaped plates in the ADAS dissipater (Kelly et al. 1972; Whittaker et al. 1989), triangular plates in the TADAS dissipater (Tsai et al. 1993), rhombic low yield strength plate (Shih and Sung 2005), and diagonal braced frame equipped with TADAS dissipater (Gray et al. 2012). Although some suggestions, such as the E-shaped dissipater (Ciampi and Marioni 1991; Tsopelas and Constantinou 1997), have been made by researchers to create a constant moment distribution in the ductile part of the dissipater, a combination of shear and flexural actions has emerged in most cases. Due to presence of shear force concurrently with bending moment in such dissipaters, width of the dissipater plate has been varied to create a constant curvature in the dissipater similar to the constant moment condition. There are many other types of yielding dissipaters with flexural mechanism including slit steel plates (Lee et al. 2002, 2015; Lee and Kim 2017; Amiri et al. 2018), J-shaped and U-shaped plates (Kato and Kim 2006; Oh et al. 2013; Tagawa and Gao 2012; Bagheri et al. 2015), pipes (Maleki and Bagheri 2010; Maleki and Mahjoubi 2013; Mahjoubi and Maleki 2016), steel rings (Andalib et al. 2014), and bending bars combined with viscoelastic materials (Banisheikholeslami et al. 2016).

In a large number of existing dissipaters, combination of different forces in a ductile member prevents optimal use of the dissipation capacity of the dissipater material and reduces ductility of the dissipater. In this paper, a new type of the yielding dissipater with a pure bending mechanism is introduced and examined both experimentally and theoretically.

The benefits of this device include high and stable energy absorption capacity, uniform force resistance in tension and compression, inexpensive maintenance, and rapid exchangeability after severe earthquakes. In this study, sixteen specimens of this type of dissipater have been tested cyclically and their structural properties have been discussed.

This paper is organized as follows. In Sect. 2, the device is introduced and the governing equations of axial yielding and ultimate axial capacity are described. An analytical model is developed in Sect. 3. In Sect. 4, the experimental program and the specifications of the proposed dissipater device are explained. The analytical model is calibrated based on the test results in Sect. 5 and its performance in predicting the hysteresis behavior is compared with the experimental results of the tested specimens. Finally, the conclusions are presented in Sect. 6.

2 The proposed energy dissipating device

A pure bending yielding dissipater (PBYD) device is developed in this study intended for use in concentric braced frames. Some possible PBYD installation configurations in concentric bracing systems are shown in Fig. 1. The same capacity of this device in tension and compression makes a single diagonal brace in each frame sufficient. Using this device in Chevron and V bracing frames significantly reduces the shear force demand on the braced bay beam due to unbalanced forces of compression and tension braces. The axial force of the bracing member caused by lateral loading is transferred to the PBYD device. The PBYD mechanism is designed such that the axial force is converted to a pure bending moment acting on the dissipater plates. The PBYD detail that transforms the axial force to pure bending in dissipater plates is shown in Fig. 2. To maintain the geometrical symmetry of the device, a four-point loading system is used to create pure bending in the middle region of the dissipater plates. Transmission of the axial force to the middle supports and from there through the dissipater plates to the lateral constraint blocks is shown in Fig. 3. In this figure, diagram of the shear force and the bending moment in the dissipater plates under axial loading are illustrated. Absence of shear force in the middle area of the dissipater plates results in pure bending in this part and causes a large amount of plate material to be yieldable simultaneously under axial loading. In order to prevent transverse movement, shear keys are used on the edges of the dissipater plates at the middle of the plate length, which is located in the grooves embedded in the upper and lower holder plates (visible in Fig. 2). Existence of these shear keys prevents instability during loading, which in turn maintains the symmetry condition in the dissipater behavior and free deformation of the dissipater plates under tensile and compressive loads.
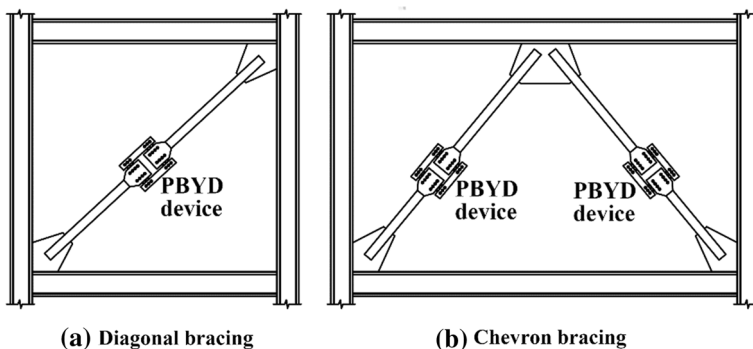

(a) Diagonal bracing   (b) Chevron bracing

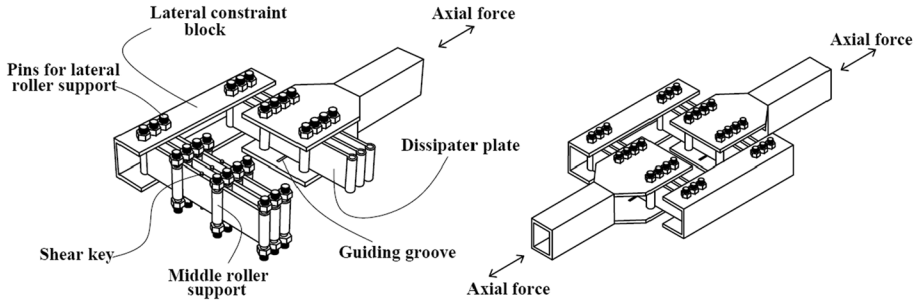**Fig. 1** Possible PBYD installation in concentric bracing

Fig. 2 PBYD details for transforming axial force to pure bending in dissipater plates
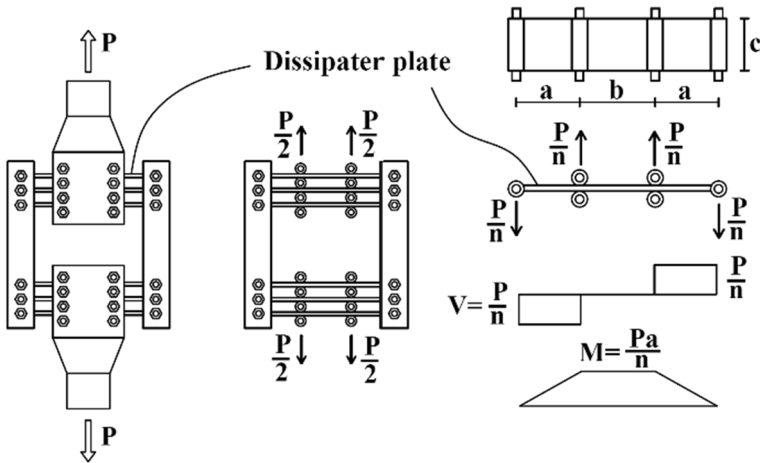

Fig. 3 Shear and moment diagrams in the dissipater plates under axial loading (n = number of plates)

By sufficiently increasing the axial force in the dissipater device, the bending stress at the middle part of the dissipater plate increases and causes the extreme fibers to reach the yield stress. The axial yielding strength (P_y) of the dissipater device can be predicted by the following equation,

$$P_y = \frac{nct^2 F_{ye}}{6a} \tag{1}$$

where F_{ye} is the plate material expected yielding stress, n is the number of dissipater plates in the device, c and t are the width and thickness of the dissipater plate, respectively, and a is the length of the side parts of the dissipater plate (Fig. 3). The material expected yielding stress (F_{ye}) is the product of the material minimum specified yield stress (F_y) and material overstrength factor R_y ($F_{ye} = R_y F_y$).

The initial axial stiffness of the dissipater device can be determined using fundamentals of the strength of materials as below,

$$k_i = \frac{nEI}{a^2 \left(\frac{2}{3}a + b \right)} \tag{2}$$

where E is the Young's modulus, b is the length of middle part (Fig. 3), and I is moment of inertia ($I = ct^3/12$) of the dissipater plate.

After initial yielding, inelastic behavior occurs in the proposed device. Strain and stress distribution in the middle part of the dissipater plate is shown in Fig. 4. The elastic and inelastic stress distributions are shown in this figure. For design purposes, the elastic–perfectly-plastic behavior (Fig. 4c) can be assumed for steel to determine the ultimate axial capacity, P_u, of the device. Effects of nonlinearities such as strain hardening in steel and large deformations should be considered in predicting the axial load capacity of the dissipater device. In this case, the overstrength factor C_p is utilized for considering the nonlinearity effects, as

$$P_u = C_p \frac{nct^2 F_{ye}}{4a} \tag{3}$$

$$C_p = \frac{F_y + F_u}{2F_y} \tag{4}$$

where F_u is the ultimate stress of steel. Accuracy of Eq. (4) to determine the overstrength factor C_p is investigated after testing.

3 The analytical model

Behavior of the proposed device is influenced by the behavior of its plates. The analytical model of the proposed dissipater should consider the effect of various factors including large deformations, nonlinear behavior of material, and the nonlinear behavior caused by slip limitation of the dissipater plate at the middle supports in large deformations. According to the shear and moment diagrams of the dissipater plates in Fig. 3, the middle part of the plates is deformed as a circular arc with a radius R even at large deformation due to the presence of pure bending. Figure 5 demonstrates the deformed shape of a dissipater plate for considering the geometrical nonlinearity. The side parts of the plate deform as cantilever beams with the rotation $\theta_{support}$ at their supports as shown in Fig. 5a. Figure 5b demonstrates a unit length element of the middle part of the plate. Due to the constant curvature at the radius R in the middle part, the maximum strain ε_0 created in the extreme fibers of the section is the same throughout the area. Figure 5b shows the relationship between the maximum strain of the middle part, ε_0, with the arc angle $\theta_{support}$ and the plate thickness t. According to Fig. 5a, deformation of the side parts of the plate consists of two portions including displacements due to rotation at the middle support, Δ_1, and bending deformation, Δ_2, under the applied force P/n, as below,
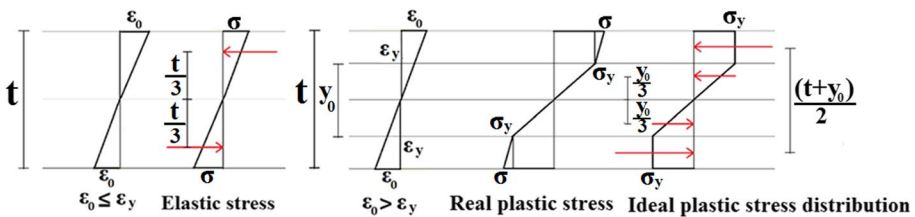

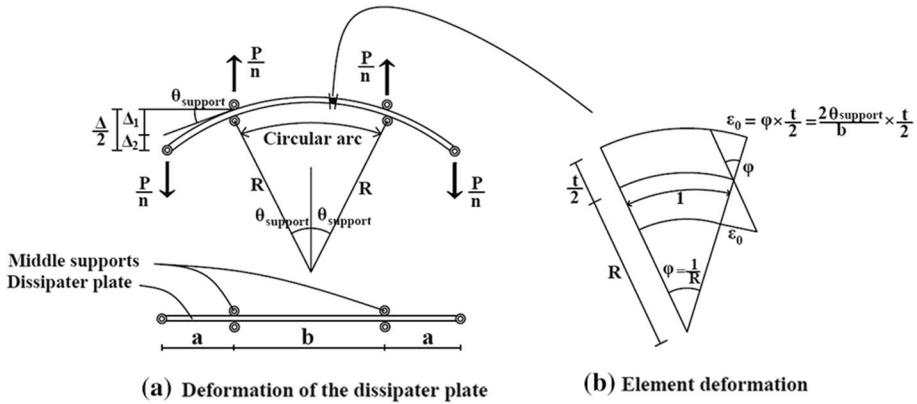**Fig. 4** Stress and strain distribution in the middle part of the dissipater plate

Fig. 5 Deformation of the dissipater plates under pure bending

$$\Delta_1 = \theta_{support} \times a = \frac{\varepsilon_0}{t} ba \tag{5}$$

$$\Delta_2 = \frac{Pa^3}{3nEI} \tag{6}$$

The two sections of the dissipater in Fig. 2 are similar to parallel springs. The overall deformation of the device, Δ, is twice the displacement of each side. It can be derived in terms of ε_0 as follows,

$$\Delta = 2(\Delta_1 + \Delta_2) = \frac{2\varepsilon_0}{t} ba + \frac{2Pa^3}{3nEI} \tag{7}$$

The maximum strain of the middle part, ε_0, can be obtained in terms of the axial force P and the displacement Δ of the dissipater device, as follows:

$$\varepsilon_0 = \frac{t}{2ba} \left(\Delta - \frac{2Pa^3}{3nEI} \right) \tag{8}$$

As shown in Fig. 3, the bending moment M in the middle part of the damper depends on the applied force P on the dissipater as:

$$M = \frac{Pa}{n} \tag{9}$$

To consider the effect of material nonlinearity, a bi-linear stress–strain relation is introduced as shown in Fig. 6. The stress distribution at the cross section of the plate, including strain hardening of the material, is shown in Fig. 4b. Relation between the bending moment, M, and the maximum strain in the middle part, ε_0, for the elastic and inelastic regions can be determined using Fig. 4, as below,

$$
\begin{aligned}
M &= \frac{ct^2}{6} F_y \left(\frac{\varepsilon_0}{\varepsilon_y} \right) & \varepsilon_0 \le \varepsilon_y \\
M &= \frac{ct^2}{12} F_y \left(3 - \left(\frac{\varepsilon_0}{\varepsilon_y} \right)^2 \right) + \frac{ct^2}{6} E^* (\varepsilon_0 - \varepsilon_y) \left(1 - \frac{\varepsilon_y}{\varepsilon_0} \right) \left(1 + \frac{\varepsilon_y}{2\varepsilon_0} \right) & \varepsilon_y < \varepsilon_0 \le \varepsilon_u
\end{aligned}
\tag{10}
$$

Fig. 6 The idealized bi-linear stress–strain path
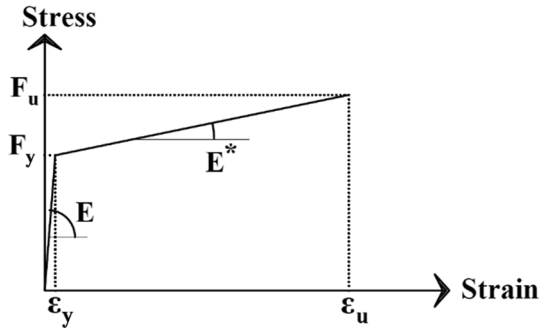
where ε_y is the yield strain, ε_u is the strain corresponding to the ultimate stress, and E^* is the modulus of the second branch (strain hardening) of the bi-linear stress–strain path. Failure will occur in this system when value of the maximum strain, ε_0, in the middle part of the plate reaches to the failure strain ε_u.

In bending of cross sections, due to presence of the Poisson's ratio v, a transverse curvature is also generated with a radius of R/v. In sections with large widths and short spans, this transverse curvature is prevented by supports. Actually, by increasing width of the beam and decreasing its span, its behavior converts to the behavior of plates in bending. This will increase bending capacity of the section. A factor α can be utilized for consideration of this effect, as follows,

$$1 \le \alpha \le \frac{1}{1 - v^2} \tag{11}$$

The lower bound of α corresponds to ordinary beams with a small width to thickness ratio (c/t) and a large span to thickness ratio (b/t). In contrast, the upper bound of α corresponds to the beams with opposite characteristics. For the dimensions used for the dissipater plates, $\alpha = 1/(1 - v^2)$ can be used with good accuracy. The Poisson's ratio, v, can be considered as 0.3 for steel.

According to Fig. 5, length of the dissipater plates between the two middle supports increases during deformations. The additional length is provided by slippage of plate on the middle supports. In turn, it prevents formation of axial force in the middle part of the plate. As the deformations increase, plate's angle of rotation at the middle support, $\theta_{support}$, increases. At large deformations, movement of the plates at the middle supports will become limited. It causes axial force development in the middle part and consequently increases the capacity of the device. Extent of limitation of slippage on the middle supports, depends on the ratio of the plate thickness to the length of the middle part, t/b. Increase of the dissipater's capacity due to this factor also depends on the geometric parameters of the dissipater plate. This effect can be considered as a coefficient β on the capacity of the damper.

The axial load P of the PBYD device can be written in terms of the maximum strain of the middle part of the dissipater plates, ε_0, as below,

$$
\begin{aligned}
P &= \alpha \left\{ \frac{nct^2}{6a} F_y \left(\frac{\varepsilon_0}{\varepsilon_y} \right) \right\} & \varepsilon_0 \le \varepsilon_y \\
P &= \alpha \left\{ \frac{cnt^2}{12a} F_y \left(3 - \left(\frac{\varepsilon_0}{\varepsilon_y} \right)^2 \right) + \frac{nct^2}{6a} E^* (\varepsilon_0 - \varepsilon_y) \left(1 - \frac{\varepsilon_y}{\varepsilon_0} \right) \left(1 + \frac{\varepsilon_y}{2\varepsilon_0} \right) \right\} & \varepsilon_y < \varepsilon_0 \le \varepsilon_r \\
P &= \alpha \beta \left\{ \frac{cnt^2}{12a} F_y \left(3 - \left(\frac{\varepsilon_0}{\varepsilon_y} \right)^2 \right) + \frac{nct^2}{6a} E^* (\varepsilon_0 - \varepsilon_y) \left(1 - \frac{\varepsilon_y}{\varepsilon_0} \right) \left(1 + \frac{\varepsilon_y}{2\varepsilon_0} \right) \right\} & \varepsilon_r < \varepsilon_0 \le \varepsilon_u
\end{aligned}
\tag{12}
$$

Fig. 7 Schematic axial load–displacement skeleton curve of the PBYD
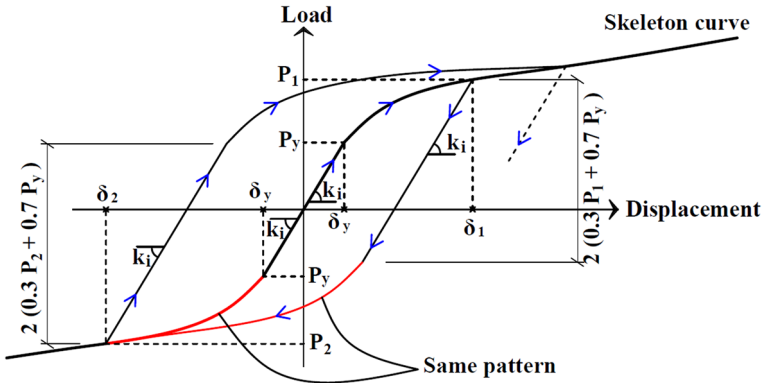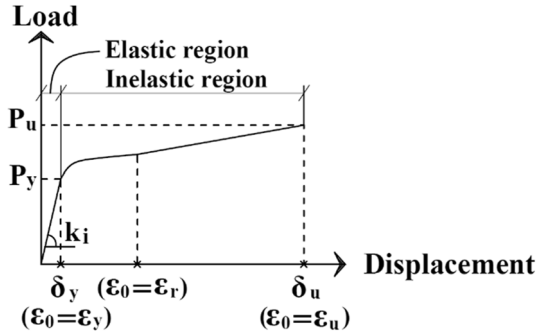

Fig. 8 The hysteretic behavior approach of the analytical model

where the strain ε_r corresponds to the beginning of movement restriction and the value of β can be considered in terms of geometric parameters of the dissipater plates, as follows,

$$\varepsilon_r = \lambda \frac{t}{b} \tag{13}$$

$$\beta = 1 + \gamma \frac{b}{ct^2}(\varepsilon_0 - \varepsilon_r) \tag{14}$$

where λ and γ are some coefficients to be calibrated based on the test results.

By substituting Eq. (8) in Eq. (12), an implicit relation can be established for determining the load–displacement curve as shown schematically in Fig. 7. This load–displacement curve is considered to be the skeleton curve of the hysteresis behavior of the device.. Numerical study of the suggested dissipater shows a hardening behavior somewhere between the isotropic and kinematic hardening rules. Based on this study, a combined rule including 0.3 isotropic and 0.7 kinematic hardening exhibits the best conformity with the experimental hysteresis. Regarding this issue, the cyclic curve of the analytical model of the proposed dissipater can be plotted using the skeleton curve and the cyclic approach of Fig. 8. In this figure, the skeleton curve is followed at the beginning of loading to the specified displacement, δ_1, and the corresponding load, P_1. By reversing the loading, the

unloading curve follows a parallel line to the initial branch with the slope k_i, up to the load $2(0.3P_1 + 0.7P_y)$. After this point, the loading curve follows the pattern of inelastic region of the skeleton curve up to the specified point (δ_2, P_2) on the skeleton curve.

4 Experimental program

An experimental program was designed to evaluate the cyclic behavior of the proposed yielding dissipater as well as to calibrate and verify the analytical model. The proposed dissipater is used as a part of a concentric braced system under cyclic loading caused by an earthquake. In this case, the brace member and consequently the dissipater device carry axial hysteretic forces. The brace is designed to carry an axial load larger than the dissipater capacity before buckling or yielding. Hence, the dissipater device can be tested independently under an axial cyclic loading.

4.1 Specimens and the standard tensile test characteristics

A total number of 16 specimens of the proposed dissipater device were prepared and tested in laboratory. In order to compare the performance of the device configured with different design parameters, the samples were designed at two levels of ultimate capacity. 11 samples were designed with an ultimate design capacity of 50 kN (specimens 1–11) and 5 samples with an ultimate design capacity of 90 kN (specimens 12–16). Equation (3) has been used to design these samples. The dissipater plates were made of St37 steel with a nominal yield and an ultimate stress of 240 and 370 MPa, respectively. Other non-ductile parts were made of St52 steel plates of 12 mm thickness with a nominal yield and ultimate stress of 360 and 520 MPa, respectively. The total weight of the specimens, consisting of the dissipater plates and non-ductile parts, vary between 120 kg (specimen 1) and 175 kg (specimen 16). In design of the specimens, Eqs. (1–3) are used considering $R_y = 1.15$ and $C_p = (F_y + F_u)/(2F_y) \approx 1.25$ for material and capacity overstrength factors, respectively. The accuracy of such assumptions is investigated afterwards during the tests.

The characteristics of the dissipater plates are determined by performing standard tensile tests on coupons of different thickness (ASTM E8-04 2004). The resulted stress–strain diagrams are illustrated in Fig. 9. In addition, experimental values of the parameters of the idealized bi-linear stress–strain curve of the material shown in Fig. 6, are listed in

Fig. 9 Stress–strain curves for the dissipater plates; tensile test results for different dissipater thicknesses and the corresponding idealized bilinear curves for the analytical model
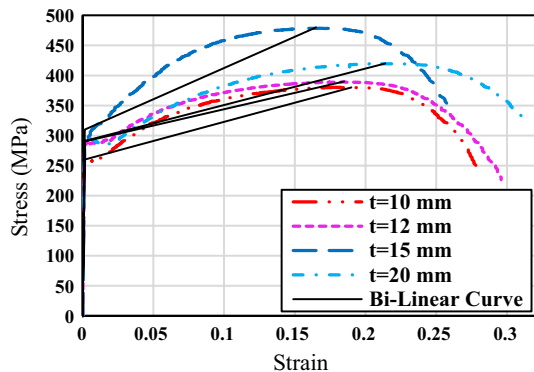
Table 1 Experimental values of the parameters of the idealized bi-linear model for material of the specimens (see Fig. 6)

Plate thickness	F_y (MPa)	F_u (MPa)	ε_y (%)	ε_u (%)	E (MPa)	E^* (MPa)
10	255.5	380.4	0.126	18.7	203,400	672
12	290.6	389.3	0.143	18.4	203,400	541
15	310.9	478.8	0.153	16.6	203,400	1021
20	290.8	419.3	0.143	21.4	203,400	605

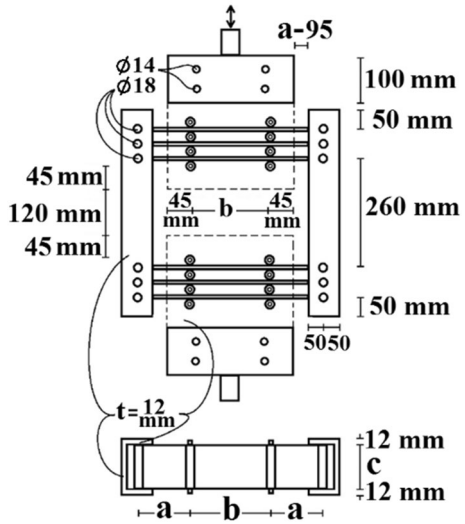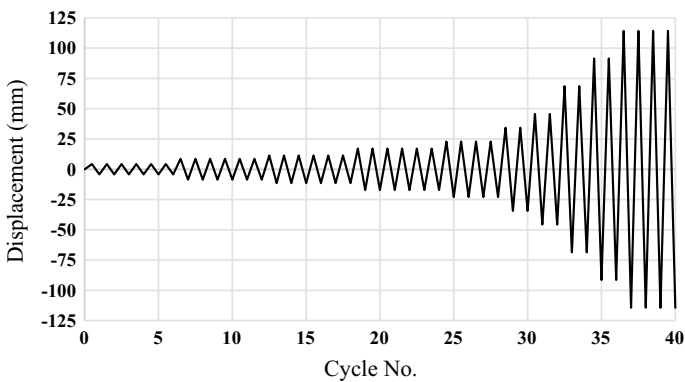**Fig. 10** Design dimensions of the dissipater device

Table 1. The tensile test gives an average modulus of elasticity of 203.4 GPa. The material overstrength factor R_y can be obtained by dividing the yield stress of the plate material observed in the test to its nominal yield stress (240 MPa). For plates with thicknesses of 10, 12, 15, and 20 mm, this ratio is calculated to be 1.06, 1.21, 1.29, and 1.21, respectively, with an average value of 1.19. This average value is 3.5% larger than the assumed value ($R_y = 1.15$) in design of the samples. The general dimensions of the PBYD device are shown in Fig. 10. The design capacities of the samples are demonstrated in Table 2. The maximum axial displacement allowance applicable to the device is equal to the distance between the two sections of the brace member that is considered to be 120 mm in design (Fig. 10). The total length of the device is about 750 mm which permits an average strain of 16% in the device at maximum applied axial displacement.

4.2 Test setup and loading history

The Santam universal testing machine with a capacity of 150 kN is used to apply the cyclic axial loading. A displacement loading protocol is applied quasi-statically to the specimens as shown in Fig. 11. The loading device is adjusted to apply a displacement rate of 250 mm/min. The test setup is demonstrated in Fig. 12. A total number of 40 loading loops with a 6000 mm cumulative displacement are applied to the specimens in this loading history. This protocol has been obtained by modifying the SAC protocol (SAC 1997) with adding 6 cycles

Table 2 Sizing of the specimens

Specimen	Number of dissipater plates	Dimensions of the dissipater plate				Design axial strength of the dissipater (P_u) (kN)
		Thick-ness (mm)	Length ($L=2a+b$) (mm)	Middle part length (b) (mm)	Width (c) (mm)	
1	6	10	363	150	103	50.0
2	6	10	413	200	103	50.0
3	6	12	453	150	102	50.2
4	4	15	458	150	103	51.9
5	4	15	511	200	101	50.4
6	6	15	619	150	103	51.1
7	6	15	672	200	103	50.8
8	6	10	463	150	153	50.6
9	4	12	452	150	153	50.3
10	6	12	603	150	152	50.0
11	4	15	624	150	153	50.1
12	6	15	461	200	102	91.0
13	4	20	460	150	103	91.7
14	6	20	611	150	102	91.6
15	6	15	543	150	153	90.7
16	4	20	610	150	152	91.2

Fig. 11 Cyclic loading history

of 0.1875% relative drift and 2 cycles of 5% relative drift to the SAC protocol. It is assumed that the PBYD device is located in a diagonal braced bay (Fig. 1) with a 3.2 m height and 3.5 m span and 5% relative drift is applied to the frame at maximum.
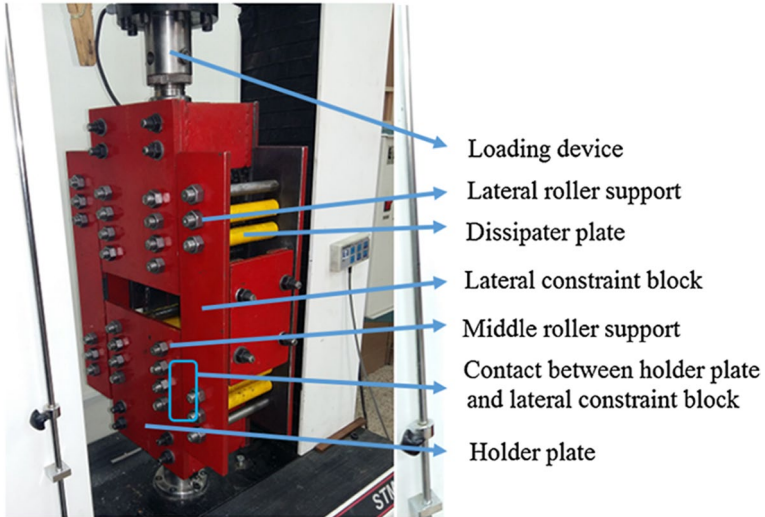
Fig. 12 Test setup

5 Results and discussion

Deformation of the plates of specimen 6 at the maximum compressive displacement is shown in Fig. 13. The hysteretic load–displacement curves of the specimens are demonstrated in Fig. 14. A summary of the test results is tabulated in Table 3.

Fig. 13 Dissipater plate deformation of specimen 6 at maximum compressive displacement
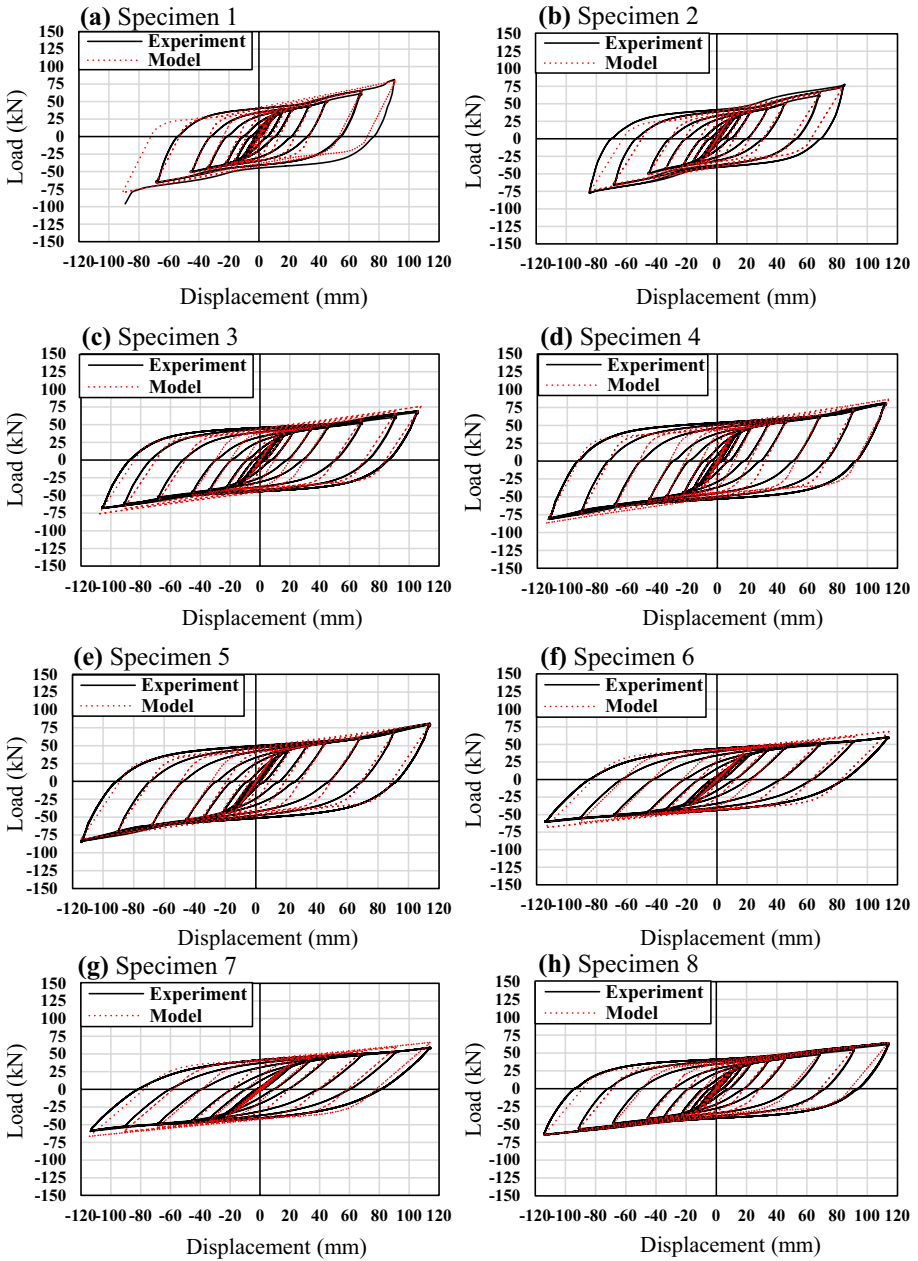
Fig. 14 Experimental load–displacement hysteresis curves and analytical predictions of the axial response of the PBYD specimens

All specimens indicate stable behavior under cyclic loading. No sign of failure or strength reduction is observed during the applied loading. The part of the dissipater plates between the middle supports (portion of the dissipater plate with constant
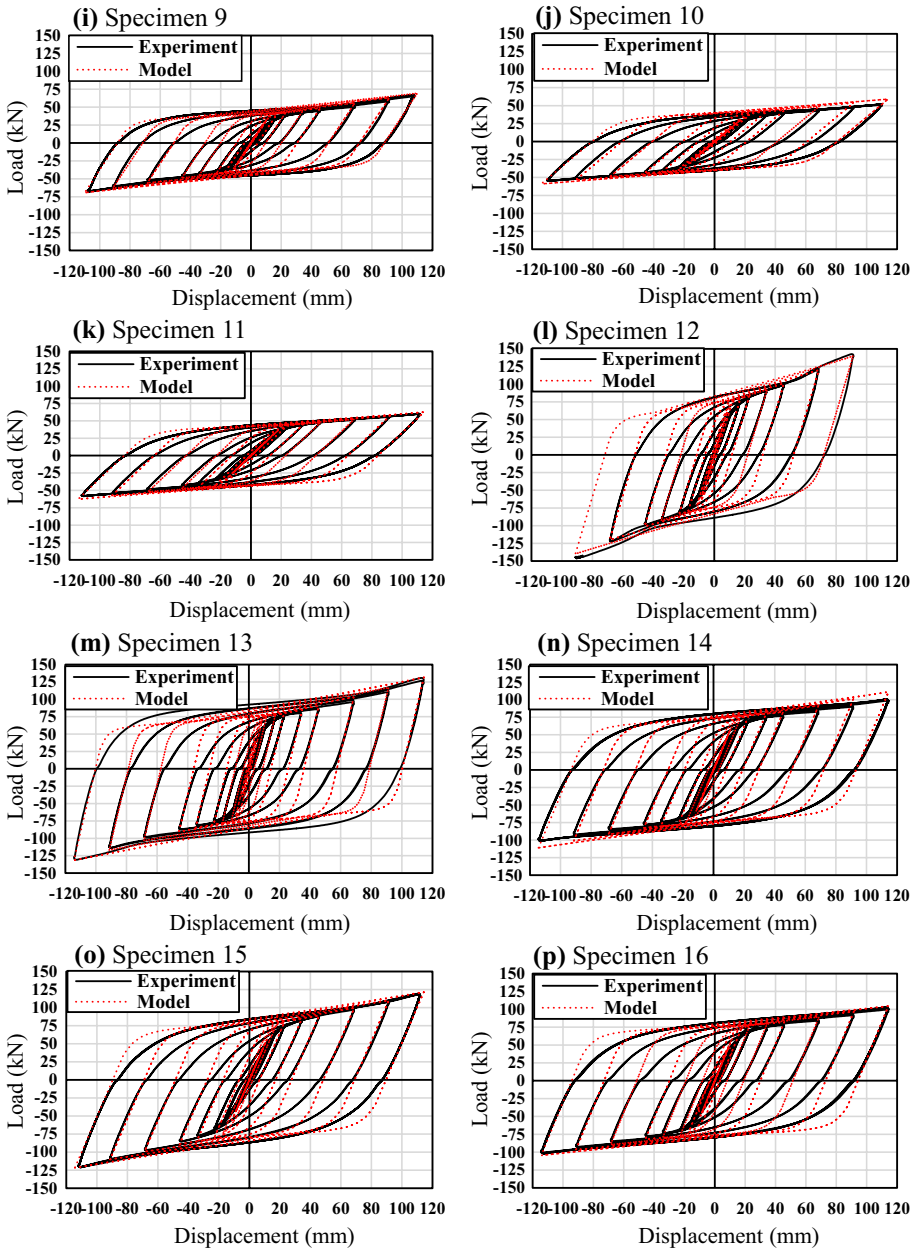
Fig. 14 (continued)

moment shown in Fig. 3) yields uniformly. Deformation in the middle part of the dissipater plates slightly increases length of plate between the two middle supports in comparison with the straight initial length (up to Δ_P in Fig. 15). Therefore, the dissipater plate slips on the middle supports to provide for the extra length. The movement marker

Table 3 Test results

| Specimen	k_i (kN/mm)	$k_f/k_{i,ex}$	P_y (kN)	$P_{y,ex}$ (kN)	$P_y/P_{y,ex}$	$\delta_{y,ex}$ (mm)	$\delta_{max,ex}$ (mm)	$\delta_{max,ex}/\delta_{y,ex}$	$P_{t,ex}$ (kN)	$P_{c,ex}$ (kN)
1	4.12	1.02	24.71	22.44	1.10	5.5	90.3	16.42	81.62	−84.34
2	3.36	1.02	24.71	22.93	1.08	7.0	85.0	12.14	77.65	−77.84
3	3.07	1.08	28.17	26.96	1.04	9.5	107.0	11.26	69.43	−68.28
4	3.70	1.02	31.19	30.45	1.02	8.4	112.8	13.43	81.77	−81.50
5	3.09	1.08	30.29	29.20	1.04	10.2	112.8	11.06	81.54	−85.57
6	1.99	1.01	30.73	30.07	1.02	15.3	112.8	7.37	60.45	−60.67
7	1.71	1.04	30.53	30.45	1.00	18.6	112.8	6.06	59.31	−59.77
8	2.47	1.06	24.98	24.94	1.00	10.7	112.8	10.54	64.23	−64.64
9	3.07	1.07	28.27	26.70	1.06	9.3	107.0	11.51	67.28	−67.80
10	1.71	0.99	28.08	26.53	1.06	15.4	112.8	7.32	51.80	−54.84
11	1.99	1.01	30.11	30.22	0.99	15.3	112.8	7.37	60.30	−58.24
12	6.97	1.05	54.68	48.84	1.12	7.4	90.3	12.20	142.50	−146.31
13	8.76	1.07	51.53	48.81	1.06	6.0	112.8	18.80	130.81	−130.74
14	4.99	1.05	51.47	48.03	1.07	10.1	112.8	11.17	100.50	−101.03
15	4.76	1.04	54.47	47.61	1.14	10.4	112.8	10.85	119.24	−121.02
16	4.99	1.07	51.25	48.45	1.06	10.4	112.8	10.85	102.69	−101.85
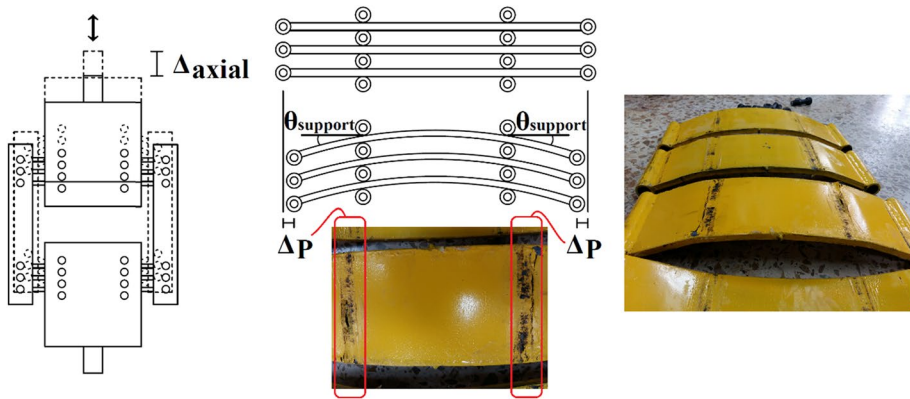
Fig. 15 Dissipater plate deformation and movement marker at the middle roller supports (specimen 1)

of the dissipater plate slippage on the middle roller supports after test of specimen 1 is obvious in Fig. 15.

Increasing the axial deformation of the PBYD device increases rotation of the dissipater plate at the middle support ($\theta_{support}$ in Figs. 5 and 15). Due to sequential placement of the dissipater plates, the significant increase in rotation of the dissipater plate at the middle support limits slippage at the roller middle supports. This event produces an axial force in the dissipater plates and results in a nonlinear increase in stiffness and strength of the dissipater device at large axial displacements. In specimen 12, strength of the device increased significantly to the values larger than the design strength of the specimen (90 kN) and reached the maximum load capacity of the apparatus (150 kN). This test was stopped to prevent damage to the test setup (visible in Fig. 14*l*). In specimens 1 and 2, the allowance between the holder plates and the lateral constraint blocks that was initially equal to 12 mm (Fig. 10), reduced to zero at a nearly 90 mm axial displacement because of the dissipater plate slippage on the middle roller supports as observed in Fig. 12. The resulting contact between the holder plates and the lateral constraint blocks increased the device strength abruptly. The corresponding tests were stopped also to prevent damage to the test setup (visible in Fig. 14a and b).

Based on comparison of the analytical results with those of the experimental tests, values of the parameters λ and γ in Eqs. 13 and 14, respectively, are calibrated to be $\lambda = 0.075$ and $\gamma = 2500$. By using these values in the equations of Sect. 3, applying the loading protocol of Fig. 11 on the skeleton curve and considering the cyclic approach of Fig. 8, the analytical cyclic curves of the force–displacement behavior of the specimens can be drawn. These curves are demonstrated alongside the test results in Fig. 14. Comparison between the experimental and analytical results confirms the fact that the analytical model can predict the cyclic response of the proposed dissipater with a very good accuracy.

5.1 Initial stiffness and yield strength

The experimental yield strength ($P_{y,ex}$) and the yield displacement ($\delta_{y,ex}$) of the specimens are shown in Table 3. The yield point is defined as the point at which there is more than 5% deviation from the initial linear relationship. Ratio of the predicted stiffness (k_i) calculated by Eq. (2) to the experimental initial stiffness ($k_{i,ex} = P_{y,ex}/\delta_{y,ex}$) is also shown in Table 3.

As seen, Eq. (2) predicts the stiffness up to 8% more than the experimental results, showing good accuracy of the equation. The cyclic load–displacement curves in Fig. 14 indicate that stiffness of the device decreases gradually after the yield point because of gradual increase of the yielding area through the thickness of the dissipater plates (Fig. 4). Hence, a sudden drop in stiffness is prevented in the proposed device. Difference between the predicted and the experimental yield strengths (P_y and $P_{y,ex}$, respectively) is less than 14%, which demonstrates the validity of Eq. (1) to predict the yield strength of the PBYD device.

5.2 Peak strength and nonlinear effects

The maximum strengths of the specimens in tension, $P_{t,ex}$, and in compression, $P_{c,ex}$, are demonstrated in Table 3. Based on this table, the PBYD device exhibits the same behavior in tension and compression. Because of the nonlinear increase in strength due to strain hardening and slippage allowance of the dissipater plates, the specimens' ultimate strength at large displacement is considerably more than the yield strength. The load–displacement curves of the samples (Fig. 14) with a significant rotation of the dissipater plate at the middle support ($\theta_{support}$ in Fig. 15), show that this rotation has a strong effect on the nonlinear increase of strength capacity of the device. This parameter can be approximated by the following relationship,

$$\theta_{support} = \arctan\left(\frac{\Delta_{axial}}{2a}\right) \tag{15}$$

where Δ_{axial} is the axial displacement applied to the PBYD device and a is the length of the side parts of the dissipater plate (Fig. 3).

To investigate the effect of this parameter, the axial displacement level of 80 mm is considered, corresponding to a 3.5% drift in the assumed design frame. Table 4 shows the

Table 4 Characteristics of the specimens to determine the design factors

Specimen	$\theta_{support,80}$ (°)	P_{design} (kN)	$P_{ex,80}$ (kN)	$P_{ex,80}/P_{design}$	$\varepsilon_{0,design}$ (%)
1	20.6	50.0	74.70	1.49	0.035
2	20.6	50.0	74.27	1.49	0.026
3	14.8	50.2	61.55	1.23	0.018
4	14.6	51.9	69.20	1.33	0.028
5	14.4	50.4	66.83	1.33	0.026
6	9.7	51.1	53.59	1.05	0.018
7	9.6	50.8	51.84	1.02	0.013
8	14.3	50.6	56.41	1.11	0.023
9	14.8	50.3	58.30	1.16	0.029
10	10.0	50.0	49.64	0.99	0.018
11	9.6	50.1	54.63	1.09	0.017
12	17.0	91.0	139.76	1.54	0.025
13	14.5	91.7	112.73	1.23	0.048
14	9.8	91.6	93.55	1.02	0.031
15	11.5	90.7	106.46	1.17	0.021
16	9.9	91.2	95.45	1.05	0.031

values of rotation of the dissipater plate at the middle support and the corresponding axial force at 80 mm axial displacement ($\theta_{support,80}$ and $P_{ex,80}$ columns of Table 4, respectively). The ultimate design force of the specimens (P_{design}) is also reported in Table 4. In design of the dissipater, only the effect of strength increase due to strain hardening is considered using C_p. Therefore, the C_p factor should be modified according to rotation of the dissipater plate at the middle supports. Comparison between values of the strength at an 80 mm displacement and the design strength of the specimens (with $C_p = 1.25$) is used to modify the C_p factor ($P_{ex,80}/P_{design}$ in Table 4). Based on the above comparison, the following over-strength factor can be utilized to design the proposed dissipater.

$$
\begin{aligned}
C_p &= \frac{F_u + F_y}{2F_y} & \theta_{support} \leq 10° \\
C_p &= \frac{F_u + F_y}{2F_y} + 0.04\left(\theta_{support} - 10°\right) & \theta_{support} \leq 10°
\end{aligned}
\tag{16}
$$

where $\theta_{support}$ is the rotation angle of the dissipater plate at the middle support calculated by Eq. (15).

5.3 Ductility

None of the specimens showed failure or decrease in strength at the maximum applied cyclic displacement. The maximum displacement has been calculated as the displacement equivalent to the assumed 5% story drift, being equal to 113 mm. Maximum strain at the middle part of the plates, $\varepsilon_{0,design}$ is calculated in Table 4 using Eq. (8). These values are substantially less than the failure strain of plate material in Fig. 9. Therefore, the ultimate tolerable displacement of the device, δ_u, and its corresponding ductility factor are larger than the values calculated at the maximum test displacement. In Table 3, ratio of the maximum displacement applied in experiment ($\delta_{max,ex}$) to the yield displacement ($\delta_{y,ex}$) is also calculated. This ratio emerges to be between 6 and 20 that indicates a very good level of ductility for the PBYD device.

5.4 Energy dissipation

According to the moment diagram of the dissipater plate (Fig. 3), the pure bending developed in the middle part of the dissipater plate leads to widespread plastic deformations in this region with considerable energy dissipation capacity. The deformed dissipater plate shown in Fig. 14 also indicates that the dissipater plate experiences large plastic deformations between the two middle supports. The dissipated energy for two design capacity levels of 50 kN and 90 kN are shown in Figs. 16 and 17, respectively, versus the cumulative displacement.

6 Conclusions

A new yielding dissipater accommodated with a pure bending mechanism (PBYD) was introduced in this paper. The PBYD device can be simply and inexpensively manufactured and easily replaced. The suggested device transforms the axial load of braces to pure bending in the weld-free middle part of the dissipater plates. It results in widespread plastic deformations at this region and energy dissipation as well. This device can be designed
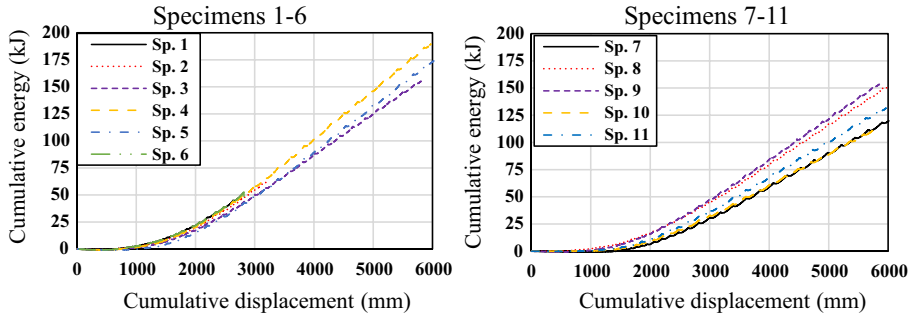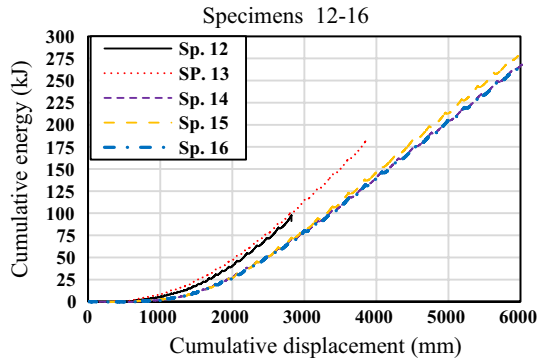
Fig. 16 Absorbed energy versus cumulative displacement for specimens with their design capacity being 50 kN

Fig. 17 Absorbed energy versus cumulative displacement for specimens with their design capacity being 90 kN

for the same structural characteristics with different dissipater plate details. Sixteen cyclic tests were conducted on independent samples of the proposed device. Specimens were designed in two different capacity groups. The load–displacement hysteresis curves demonstrate a stable behavior for all PBYD specimens. Also, the same behavior in compression and tension was observed for the proposed device. The specimens of the proposed device exhibited large displacement capacities and capability to sustain large number of cycles. No sign of failure or stiffness degradation was observed in the specimens at the maximum applied cyclic displacement (a displacement equivalent to 5% drift in the corresponding frame). The suggested device showed proper ductility at the test displacement range. The initial stiffness and yield strength of the specimens were properly predicted by the analytical equations. The overstrength design factors including R_y and C_p were investigated in this study to evaluate the ultimate strength in design of the PBYD device. Also, an analytical model was developed to predict the cyclic load–displacement curve of the suggested system considering geometrical and material nonlinearities. The analytical model was calibrated using the experimental results to consider the nonlinear effects of limitation in slippage of the plates at the middle supports for large displacements. A very good agreement was observed between the analytical and experimental results.

References

Amiri HA, Najafabadi EP, Estekanchi HE (2018) Experimental and analytical study of block slit damper. J Constr Steel Res 141:167–178

Andalib Z, Kafi MA, Kheyroddin A, Bazzaz M (2014) Experimental investigation of the ductility and performance of steel rings constructed from plates. J Constr Steel Res 103:77–88

ASTM E8-04 (2004) Standard test methods for tension testing of metallic materials. American Society for Testing and Materials (ASTM), Pennsylvania

Bagheri S, Barghian M, Saieri F, Farzinfar A (2015) U-shaped metallic-yielding damper in building structures: seismic behavior and comparison with a friction damper. Structures 3:163–171

Banisheikholeslami A, Behnamfar F, Ghandil M (2016) A beam-to-column connection with visco-elastic and hysteretic dampers for seismic damage control. J Constr Steel Res 117:185–195

Black C, Makris N, Aiken I (2004) Component testing, seismic evaluation and characterization of buckling-restrained braces. J Struct Eng 130:880–894

Calado L, Proença JM, Espinha M, Castiglioni CA (2013) Hysteretic behaviour of dissipative bolted fuses for earthquake resistant steel frames. J Constr Steel Res 85:151–162

Chan R, Albermani F, Kitipornchai S (2013) Experimental study of perforated yielding shear panel device for passive energy dissipation. J Constr Steel Res 91:14–25

Cheng FY, Jiang H, Lou K (2008) Smart structures: innovative systems for seismic response control. CRC Press, New York

Ciampi V, Marioni A (1991) New types of energy dissipating devices for seismic protection of bridges. In: Proceedings of the 3rd World Congress on Joint Sealing and Bearing Sys for Concrete Struct 1225-1245, State Univ of New York at Buffalo, New York

Deng K, Pan P, Li W, Xue Y (2015) Development of a buckling restrained shear panel damper. J Constr Steel Res 106:311–321

Formisano A, Lombardi L, Mazzolani FM (2016) Perforated metal shear panels as bracing devices of seismic-resistant structures. J Constr Steel Res 126:37–49

Franco JM, Cahís X, Gracia L, López F (2010) Experimental testing of a new anti-seismic dissipator energy device based on the plasticity of metals. Eng Struct 32:2672–2682

Gray M, Christopoulos C, Packer J, De Oliveira C (2012) A new brace option for ductile braced frames. Mod Steel Constr 52(2):40–43

Hitaka T, Matsui C (2003) Experimental study on steel shear wall with slits. ASCE J Struct Eng 129:586–595

Kato S, Kim YB (2006) A finite element parametric study on the mechanical properties of J-shaped steel hysteresis devices. J Constr Steel Res 62(8):802–811

Kelly JM, Skinner RI, Heine AJ (1972) Mechanisms of energy absorption in special devices for use in earthquake resistant structures. Bull N Z Soc Earthq Eng 5(3):63–88

Lee J, Kim J (2017) Development of box-shaped steel slit dampers for seismic retrofit of building structures. Eng Struct 150:934–946

Lee HM, Oh HS, Huh C, Oh SY, Yoon HM, Moon ST (2002) Ultimate energy absorption capacity of steel plate slit dampers subjected to shear force. Steel Struct 2:71–79

Lee CH, Ju YK, Min JK, Lho SH, Kim SD (2015) Non-uniform steel strip dampers subjected to cyclic loadings. Eng Struct 99:192–204

Mahjoubi S, Maleki S (2016) Seismic performance evaluation and design of steel structures equipped with dual-pipe dampers. J Constr Steel Res 122:25–39

Maleki S, Bagheri S (2010) Pipe damper, part I: experimental and analytical study. J Constr Steel Res 66:1088–1095

Maleki S, Mahjoubi S (2013) Dual-pipe damper. J Constr Steel Res 85:81–91

Nakashima M, Iwai S, Iwata M, Takeuchi T, Konomi S, Akazawa T et al (1994) Energy dissipation behaviour of shear panels made of low yield steel. Earthq Eng Struct Dyn 23:1299–1313

Oh SH, Song SH, Lee SH (2013) Experimental study of seismic performance of base-isolated frames with U-shaped hysteretic energy-dissipating devices. Eng Struct 56:2014–2027

Ozcelik R, Dikiciasik Y, Erdil EF (2017) The development of the buckling restrained braces with new end restrains. J Constr Steel Res 138:208–220

Piedrafita D, Cahis X, Simon E, Comas J (2013) A new modular buckling restrained brace for seismic resistant buildings. Eng Struct 56:1967–1975

Piedrafita D, Cahis X, Simon E, Comas J (2015) A new perforated core buckling restrained brace. Eng Struct 85:118–126

SAC (1997) Protocol for fabrication, inspection, testing and documentation of beam-colum connection tests and other experimental specimens. Report No. SAC/BD-97/02, SAC Joint Venture, California

Shih MH, Sung WP (2005) A model for hysteretic behavior of rhombic low yield strength steel added damping and stiffness. Comput Struct 83:895–908

Skinner RI, Kelly JM, Heine AJ (1975) Hysteretic dampers for earthquake-resistant structures. Earthq Eng Struct Dyn 3:287–296

Soong TT, Dargush GF (1997) Passive energy dissipation systems in structural engineering. Wiley, USA

Speicher MS, DesRoches R, Leon RT (2011) Experimental results of a NiTi shape memory alloy (SMA)-based recentering beam-column connection. Eng Struct 33:2448–2457

Tabatabaei SAR, Mirghaderi SR, Hosseini A (2014) Experimental and numerical developing of reduced length buckling-restrained braces. Eng Struct 77:143–160

Tagawa H, Gao J (2012) Evaluation of vibration control system with U-dampers based on quasi-linear motion mechanism. J Constr Steel Res 70:213–225

Tsai KC, Chen HW, Hong CP, Su YF (1993) Design of steel triangular plate energy absorbers for seismic-resistant construction. Earthq Spectra 9(3):505–528

Tsopelas P, Constantinou MC (1997) Study of elastoplastic bridge seismic isolation system. J Struct Eng 123(4):489–498

Vetr MG, Ghamari A (2012) Improving of seismic performance of steel structures using an innovative passive energy dissipation with torsional mechanism. Int J Civil Environ Eng 12(5):63–69

Whittaker A, Bertero V, Alonso J, Thompson C (1989) Earthquake Simulator Testing of Steel Plate Added Damping and Stiffness Elements. Report No. UCB/EERC-89/02, Earthquake Engineering Research Center, University of California, Berkeley